Deep postseismic viscoelastic relaxation excited by an intraslab normal fault earthquake in the Chile subduction zone

Lidong Bie[*1], Isabelle Ryder[1], Marianne Metois[2]

[1]School of Environmental Sciences, University of Liverpool, UK.

[2] Univ Lyon, Université Lyon 1, Ens de Lyon, CNRS, UMR 5276 LGL-TPE, F-69622, Villeurbanne, France.

E-mail: l.bie@liv.ac.uk

Abstract

The 2005 M_w 7.8 Tarapaca earthquake was the result of normal faulting on a west-dipping plane at a depth of ~ 90 km within the subducting slab down-dip of the North Chilean gap that partially ruptured in the 2014 M 8.2 Iquique earthquake. We use Envisat observations of nearly four years of postseismic deformation following the earthquake, together with some survey GPS measurements, to investigate the viscoelastic relaxation response of the surrounding upper mantle to the coseismic stress. We constrain the rheological structure by testing various 3D models, taking into account the vertical and lateral heterogeneities in viscosity that one would expect in a subduction zone environment. A viscosity of 4 - 8 × 10^{18} Pa s for the continental mantle asthenosphere fits both InSAR line-of-sight (LOS) and GPS horizontal displacements reasonably well. In order to test whether the Tarapaca earthquake and associated postseismic relaxation could have triggered the 2014 Iquique sequence, we computed the Coulomb stress change induced by the co- and postseismic deformation following the Tarapaca earthquake on the megathrust interface and nodal planes of its *M* 6.7 foreshock. These static stress calculations show that the Tarapaca earthquake may have an indirect influence on the Iquique earthquake, via loading of the *M* 6.7 preshock positively. We demonstrate the feasibility of using deep intraslab earthquakes to constrain subduction zone rheology. Continuing geodetic observation following the 2014 Iquique earthquake may further validate the rheological parameters obtained here.

Keywords: Tarapaca, subduction zone rheology, viscoelastic relaxation, normal faulting earthquake, geodetic observation

1. Introduction

One of the key factors that limit our understanding of the physics governing megathrust earthquake cycles is a lack of knowledge of subduction zone rheology. Theoretically, stresses induced by megathrust earthquakes will be relaxed in thermally weakened layers. Postseismic deformation produced by this viscoelastic relaxation process (VER) may be modeled to constrain the rheology. Recent advances in the spatial and temporal coverage of geodetic measurements have allowed for transient deformation following several megathrust earthquakes being explicitly investigated to infer rheological properties at various subduction zones (e.g.

Pollitz et al., 2008; Hu & Wang 2012; Sun et al., 2014; Trubienko et al., 2014; Klein et al., 2016).

Intermediate depth earthquakes represent another type of event in subduction zones that ruptures within the subducting slab at depths of 70 to 300 km. Large intermediate-depth earthquakes also induce stresses, which will gradually be relaxed by VER in the adjoining mantle, and produce transient deformation that could be indicative of subduction zone rheology. To test the feasibility of using intermediate depth earthquakes to constrain subduction zone rheology, we investigate InSAR and GPS observations following the June 13, 2005 magnitude 7.8 Tarapaca earthquake, which occurred ~ 100 km inland from the coast in northern Chile (Fig. 1). Seismological and geodetic studies identified this event as a slab-pull normal faulting earthquake on a shallowly west-dipping intraslab fault at ~ 90 km depth (Peyrat et al., 2006; Delouis & Legrand, 2007).

In this region, the Nazca plate subducts beneath the South American plate at a rate of ~ 7 cm/yr (Argus et al., 2011). Studies of interseismic deformation show that this segment of the plate boundary is overall highly locked, with a local decrease of coupling in front of Iquique (e.g. Chlieh et al., 2011; Béjar-Pizarro et al., 2013; Métois et al., 2013). In April 2014, the magnitude 8.2 Iquique earthquake occurred ~ 100 km offshore and partially released the strain accumulated on the shallow interface since the last big earthquake in 1877 (e.g. Ruiz et al., 2014; Schurr et al., 2014; Bürgmann 2014). Two weeks before the mainshock, a M6.7 foreshock ruptured at shallow depth of ~12 km (Fuenzalida et al., 2014). The spatial and temporal closeness of the 2014 Iquique earthquake and the 2005 Tarapaca earthquake raised the question about whether there is any link between the intraslab earthquakes and megathrust earthquakes. We assess the static stress change brought about by the 2005 Tarapaca earthquake and subsequent VER, and explore whether the 2014 Iquique earthquake, or the energetic foreshock sequence in the preceding months, may have been triggered by the 2005 Tarapaca earthquake.

2. Surface deformation data

2.1 InSAR data

We collect all postseismic SAR images from the C-band Envisat satellite spanning ~ 4 yrs from July 2005 to August 2009. In total, 29 SAR acquisitions from track 96 are processed, each with a swath nearly 500 km long, large enough to give a good coverage of the potential VER-induced long-wavelength ground displacement. Given the relatively arid regional environment and sparse vegetation, the coherence is generally good, leading to a total of 135 interferograms produced using the JPL/Caltech software ROI_PAC (Rosen et al., 2004). Topographic phase is removed using the 3-arc-second DEM from the Shuttle Radar Topography Mission (Farr et al., 2007). The interferograms are unwrapped using a branch-cut method (Goldstein & Werner, 1998).

The detection of low-amplitude, long-wavelength postseismic signals has in general been limited by atmospheric delays and imprecise orbits (Jolivet et al., 2014). To mitigate the atmospheric delay effect, we adopt the method described by Walters et al. (2013) and Jolivet et al. (2014). We estimate the phase delay caused by water vapor difference using data from the Medium-Resolution Imaging Spectrometer (MERIS) instrument aboard the Envisat satellite, and that caused by spatial variation of atmospheric pressure using the ERA-Interim global atmospheric model provided by the European Centre for Medium-Range Weather Forecasts (ECMWF). The effective use of MERIS data requires largely cloud-free (< 25 % cloud) weather conditions, which constrains the number of usable interferograms to 45 (Fig. S1 and Table S2). After correction for atmospheric noise, uncertainties associated with the satellite orbits are removed assuming a linear phase ramp across the interferogram. Removal of a linear ramp should not compromise postseismic viscoelastic signal, given the linear assumption along the whole track of data, although the effect of plate interface creep may be reduced.

Given the depth of the earthquake (~ 90 km), any postseismic signal is expected to be small (i.e. few millimetres). Considering the low signal-to-noise ratio, we chose to build a deformation rate map, rather than a time-series. The rate map is produced by averaging the added phase of 45 noise-corrected interferograms over their total time span. Out of the 45 interferograms, pixels coherent in at least 40 interferograms are stacked to produce a rate map.

The rate map shows two notable features (Fig. 2). One is the circular negative line-of-sight change associated with activity at Sillajhuay volcano, with a peak rate of ~ 1.4 cm/yr. The other feature is a broad-scale negative millimeter-level line-of-sight change over the area of the coseismic rupture. The postseismic range decrease is in contrast to the circular zone of subsidence that occurred coseismically (Peyrat et al., 2006). This contrast of coseismic and postseismic displacement is a first hint that the postseismic relaxation mechanism is VER. In Section 3 below, we run models to explore whether VER is a viable mechanism.

2.2 GPS data

In this study, we take advantage of the long-standing campaign measurements of the GPS network installed by Chilean and French teams in North Chile starting in the 1990's (Ruegg et al., 1996). One profile composed of nine benchmarks traverses the epicentral area of the Tarapaca earthquake (Ruegg et al., 1996; Chlieh et al., 2004; Métois et al., 2013) from the coast to the vicinity of Sillajhuay volcano in a northeast direction (Fig. 1). Measurements have been conducted on this network before the Tarapaca earthquake, in 1996 and 2000, with an additional measurement in 2002 for two stations (Table S3). The next survey was carried out in the month following the Tarapaca earthquake, and subsequent measurements were conducted in 2010 and 2012 (Table S4).

We process all these data following the method described in Métois et al. (2013) using the GAMIT-GLOBK software (King & Bock 2002), and obtain horizontal velocities before and after the 2005 Tarapaca earthquake (Fig. 3a, and Table S3 & S4). Velocities calculated first in the ITRF 2008 (Altamimi et al. 2011) are then rotated into a fixed South America reference frame as defined by the pole from the NNR Nuvel-1A model (DeMets Gordon 1994).

The large uncertainties associated with the pre-Tarapaca velocities (Table S3) are mostly due to the bad quality of orbits and reference-frame stations prior to 1997, to poor-quality antenna calibration models, and to the fact that the observation sessions were often shorter than an entire day (in particular for the first 1996 campaign). However, the large time span covered by the campaigns gives us confidence in these velocities. We observe a significant difference between the pre- and post-Tarapaca velocities (Fig. 3b and Table S5). The residual velocities are systematic and produce a divergent pattern away from the epicentral area (Fig. 3b). We interpret this change in velocity before and after the Tarapaca earthquake as mostly due to the postseismic VER following the mainshock. However, part of this residual motion could be due to afterslip following the mainshock, or due to changes in the degree of interseismic coupling on the plate interface. The divergent pattern centred on the Tarapaca epicentre speaks in favor of a signal dominated by postseismic VER, and we will test this hypothesis in the following modelling section.

3. Modelling

3.1 VER modelling

Seismic tomography studies in this region reveal two important features of the subduction zone rheology. The first is a uniform low P-wave attenuation for the forearc, extending eastward to longitude -69°. In accordance with low surface heat flow values, the low attenuation indicates a cold and stagnant forearc. The second is a ~ 45 km-thick layer beneath the magmatic arc with high P-wave attenuation, interpreted as being composed of partial melts ascending from mantle asthenosphere (Schurr et al., 2003). The 2005 Tarapaca earthquake occurred within the subducted rigid oceanic lithosphere. Given its proximity to the weak layer, there is a good chance that any coseismic stress perturbation excited a VER process. To model the VER-induced surface displacement, we used the software RELAX, a 3-D semi-analytic package which can incorporate lateral rheological heterogeneity (Barbot & Fialko 2010).

Our model configuration is shown on a cross section perpendicular to the trench in Fig. 4. The elastic layers of the continental and subducted oceanic lithosphere are both set to have a thickness of 40 km. A Poisson's ratio of 0.25 is assumed, and a uniform shear modulus of 63.4 GPa is set for the entire model (Hetland & Zhang 2014). As an input, the coseismic slip model we adopted is from Peyrat et al. (2006), as summarized in Table S1. Assuming a Maxwell viscoelastic rheology, we fixed the oceanic mantle viscosity at 1×10^{20} Pa s, which is similar to the global mantle average (Moucha et al., 2007), as used by Wang et al. (2012). Forward modelling tests show that decreasing the viscosity of the oceanic mantle increases the RMS misfit (Fig. S2). The rheological parameters we aimed to constrain include the size of the strong forearc H_A (zone A), the thickness H_B and viscosity η_B of the weak layer below the magmatic arc (zone B), and the viscosity of the area η_C (zone C) beneath zone B (Fig. 4).

In order to obtain a model that fits the first-order spatial pattern as revealed by InSAR observations, we progressively test various 3D rheological models in four steps (Fig. 5). For each step, the root-mean-square (RMS) misfit is plotted against the parameter we are trying to constrain. Here, the area of Sillajhuay volcano is masked out before calculating RMS, to avoid the potential influence of volcanic deformation on the RMS computation. In the first step, we infer the best-fit size of zone A, treated as elastic, while keeping the viscosities η_B of zone B and η_C of zone C as 4×10^{18} Pa s. Then, in the second step, we vary the thickness H_B of zone B and find that a value between 40 km and 50 km fits the observations well. In this step, zone B is taken to be an elastic layer. We note that, the best fit thickness found in the second step is in its lower limit, given the elastic assumption of zone B. Subsequently, we test different viscosities η_C for zone C, and a viscosity of 8×10^{18} Pa s gives a minimum RMS (Fig. 5c). Finally, we iterated the modelling with various viscosities for zone B, and found a lower bound viscosity η_B of 5×10^{19} Pa s, since lower values rapidly increase the RMS misfit (Fig. 5d). After finding the optimal values for each parameter, we fixed the η_B and η_C as 5×10^{19} Pa s and 8×10^{18} Pa s, respectively, and repeated the first step, to identify if the thickness for zone A stays at the optimal value. This test (Fig. S3) shows a minimum RMS misfit at 45 km, suggesting consistency with our optimal model. We also test for a viscoelastic zone A, by decreasing its viscosity to the same value (4 x 10^{18} Pa s) as zones B and C. In this case, the predicted displacement pattern differs markedly from the observations, showing an opposite sign of range change (Fig. S4).

To validate our model, we compare the forward-modelled horizontal displacements with the GPS data, which is the difference between the interseismic velocity before and postseismic velocity after the Tarapaca earthquake. As shown in Fig. 6(a), the InSAR-derived viscosity η_C of 8×10^{18} Pa s for zone C gives a very good azimuthal fit to the GPS displacements, but the amplitudes are under-predicted. The azimuthal alignment demonstrates that VER contributed at least part of the GPS-recorded postseismic deformation. A model conducted with a lower viscosity η_C of 4×10^{18} Pa s better fits the amplitude of the GPS data, but produces a systematic anti-clockwise bias in azimuth for sites located northeast of the fault (Fig. 6b). We note that the RMS calculated for the InSAR data differ less than 0.025 cm/yr for models with viscosities η_C of 4×10^{18} and 8×10^{18} Pa s. With a lower viscosity in zone C, the predicted InSAR displacement is slightly larger in amplitude in comparison to the observations (Fig. S5). We further discuss this relative inconsistency between InSAR and GPS data in Section 4.1.

3.2 Static stress change modelling

Static stress transfer is one of the mechanisms that can explain the occurrence of earthquakes following other events. In addition to coseismic stress changes, postseismic processes such as viscoelastic relaxation also modify the stress loading on surrounding faults (Steacy et al., 2005). The 2014 Iquique earthquake and its main *M* 6.7 preshock occurred about 9 years after the 2005 Tarapaca earthquake. The proximity of these events both in space (Fig. 1) and time offers a good opportunity to evaluate the possibility of static stress triggering.

To do so, we calculate the Coulomb stress change caused by the Tarapaca earthquake and its postseismic VER process on the subduction shallow interface and preshock nodal planes, based on the equation:

$$\Delta\sigma_f = \Delta\tau + \mu'\Delta\sigma_n$$

where $\Delta\tau$ and $\Delta\sigma_n$ are shear and normal stress changes, and μ' is the apparent friction. We assume a value for μ' of 0.4, and note that changing this value does not affect qualitatively the stress loading pattern. Details of coseismic rupture and viscoelastic relaxation induced stress change are discussed in Section 4.3.

We choose the 2014 Iquique rupture plane from the coseismic model proposed by Hayes et al. (2014). As there is currently no consensus on the rupture plane of the *M* 6.7 preshock, we projected stress changes onto both nodal planes derived from moment tensor inversion by Fuenzalida et al. (2014). Fig. 7(a) shows the Coulomb stress change superimposed on the slip models for the Iquique earthquake and its largest aftershock, and the aftershock distribution from Schurr et al. (2014). It is apparent that most aftershocks and the majority of slip locate in a negative stress zone, implying a lack of direct triggering effect for the mainshock. Stresses resolved onto the two pre-shock nodal planes show a positive loading on the shallow NNE-dipping one (Fig. 7c). Hayes et al. (2014) propose that the *M* 6.7 preshock imparted a positive stress on the plate interface where the *M* 8.2 Iquique earthquake occurred. We further propose here that the 2005 Tarapaca earthquake may have acted as an indirect trigger of the 2014 Iquique earthquake, via loading on the preshock.

4. Discussion

4.1 Likely sources of uncertainties

In this study, we have used an intermediate-depth intraslab normal faulting earthquake to constrain the northern Chile subduction zone rheological structure. Our models successfully retrieve the first-order spatial pattern of the geodetically-recorded surface deformation. While a model with a viscosity of 8×10^{18} Pa s for zone C fits well the InSAR displacement and GPS horizontal direction, it underpredicts the GPS amplitude. Decreasing the viscosity for zone C to 4×10^{18} Pa s increases the RMS misfit between InSAR model and data by ~ 0.025 cm/yr, but the fit in GPS amplitude is improved. This inconsistency may be accounted for by several sources of uncertainty.

The first source of uncertainty comes from the modelling assumption. We notice that, the difference between observed and modelled GPS interseismic rate shows an increasing trend in amplitude towards the coastal stations (Fig. 6b), indicating a contribution from shallower process than deep VER. Given our model is constrained only by InSAR data, of which the observation of postseismic deformation starts more than one months after the earthquake, the early afterslip following the Tarapaca earthquake may have much less effect on the InSAR postseismic observations. GPS campaign observations start one week following the earthquake, which have greater chance in mapping early afterslip on the normal fault. In addition to afterslip, the assumption that the GPS-recorded difference of interseismic velocity is merely caused by the post-Tarapaca VER effect excludes a possible change in subduction zone coupling. Temporal variation in interseismic coupling has been seen in other subduction zones, for example, on the Nicoya subduction interface (Feng et al., 2012) and at northeastern Japan (e.g. Mavrommatis et al., 2014; Nishimura et al., 2004, Loveless & Meade 2016), and could occur also in North Chile as suggested by Ruiz et al. (2014). In our case, the degree of coupling may change as a result of stress perturbation due to the Tarapaca earthquake and its postseismic VER process, and/or the physical properties of the plate interface itself. Based on the above discussion, our modelling strategy in this study using only InSAR postseismic deformation to constrain the rheology brings down the effect from other postseismic processes and/or temporal variations in coupling on the plate interface.

The second source of uncertainty is related to the regional complexity in rheology. In our model, we did not consider possible viscosity heterogeneity in the along-strike direction. As shown in seismic tomography studies (see fig. 5 in Schurr et al., 2003), seismic attenuation varies at different latitudes, indicating heterogeneous rheology. The heterogeneity can also be inferred from profiles drawn parallel to the satellite flight direction across the deformed area. As shown in Fig. 8, decreasing the viscosity for zone C produces a better fit to the data on the left hand-side (corresponding to the southern part), while on the right hand side (northern side), the model deviates from the data. It suggests a likely increase of viscosity from south to north. Our models with uniform asthenospheric viscosity 8×10^{18} Pa s and 4×10^{18} Pa s could potentially act as two end-member situations, demonstrating that a slight change in viscosity can alter the observable deformation.

Third, given the low signal-to-noise ratio, any correction for noise in the InSAR data could potentially introduce extra errors by overestimating/underestimating the atmospheric contribution and phase ramp. As suggested by Bennartz & Fischer (2001), the theoretical accuracy of MERIS water vapor retrieval is 0.16 cm, which equals ~ 1.1 cm of uncertainty in the Envisat look direction. Li et al. (2006) also find that the standard deviation of the difference between MERIS water vapor retrieval and GPS-measured zenith delay is 0.11 cm, corresponding to ~ 0.74 cm of atmospheric delay. Stacking of interferograms further reduces the atmospheric noise, and thus improves the theoretical accuracy of the rate map by $N^{-0.5}$, where N denotes the number of interferograms being stacked (Zebker et al., 1997). Assuming a similar error for each interferogram used in this study, the theoretical error of our rate map is ~ 0.17 cm/yr or ~ 0.12 cm/yr, based on the MERIS accuracy reported by Bennartz & Fischer (2001) and Li et al. (2006), respectively (Fig. 8). In comparison to the reported uncertainties of MERIS water vapor retrieval, a RMS misfit of ~ 0.15 cm/yr between our model using 4×10^{18} Pa s for zone C and the rate map is not significant. Taking the above factors into consideration, in addition to the large uncertainties associated with the pre-Tarapaca GPS velocities, we suggest a likely range of viscosity of 4 - 8 $\times 10^{18}$ Pa s rather than stating a definite value.

4.2 Subduction zone rheology

Despite the uncertainties discussed above, our modelling constrains the local rheological structure in several aspects. The forearc (zone A), bordered to the east by a relatively weak lower crust and mantle lithosphere, must have high strength. Our model also requires that the lower crust and mantle lithosphere are at least an order of magnitude stronger than the asthenosphere beneath. Synthetic tests with low viscosity for zones A and B produce a different sense of motion at the surface, incompatible with the observations (Fig. S4).

Our inference of an asthenospheric viscosity of 4 - 8 $\times 10^{18}$ Pa s is consistent with estimates from recent postseismic studies of megathrust earthquakes. Klein et al. (2016) investigated the GPS-recorded postseismic deformation following the 2010 Maule earthquake in Chile, and obtained a Maxwell viscosity of 3×10^{18} Pa s for the asthenospheric mantle. In the study of postseismic deformation following the 1960 *M* 9.5 Valdivia, Chile earthquake, Ding & Lin (2014) obtained four increasing asthenosphere viscosities corresponding to four different observation periods after the earthquake. Their minimum value of 2×10^{18} Pa s, derived from the first four years of observation right after the earthquake, agrees well with the viscosity we inferred from the same period of observation after the Tarapaca earthquake. This consistency validates our estimation of the short-term viscosity by fitting the averaged early postseismic deformation over a short time scale (~ 4 yrs in both cases), although we agree with the likely non-linear stress-dependency of viscosity in the long term (Bürgmann & Dresen, 2008). An effective way to further test and modify current models of rheological structure would be to investigate postseismic deformation following the 2014 Iquique earthquake.

The regional rheological model inferred from geodetic observation shows consistency with independent constraints from seismic attenuation studies, especially in the contrast between the viscosity of zone A and B. Schurr & Rietbrock (2004) proposed that a strong forearc nose (zone A) acts as a barrier that obstructs the trenchward flow of hot asthenospheric mantle, and thus restricts the volcanic front to the east. This is consistent with the numerical thermal modelling by Wada & Wang (2009), which highlights the role of decoupling between slab and mantle wedge at depth of ~ 80 km in the formation of stagnant cold fore arc. According to the linearity of the volcanic front along the slab depth contour of ~ 90 km in northern Chile, we suggest that, in this part of the subduction zone, a strong forearc nose may be a common structure that sits on top of the subducted slab to a depth of ~ 90 km.

4.3 Interplay of different earthquake types in a subduction zone environment

Stress transfer has been successful in explaining the occurrence of megathrust earthquakes in subduction zone earthquake cycles (e.g. Ding & Lin 2014). When considering stress transfer between different phases of each cycle, it is also necessary to consider the roles played by other types of earthquakes that occur within the subduction zone. Large intraslab normal fault earthquakes are expected at the downdip edge of the coupled subduction segment (Astiz et al., 1988; Lay et al., 1989). Previous studies focused mainly on how the normal fault events themselves interact with the megathrust earthquake cycle (e.g. Kausel et al., 1992; Gardi et al., 2006). Here, we also investigated the stress loading due to VER processes following large intraslab events.

In the case of the Tarapaca earthquake, the coseismic-only stress loading is heterogeneous across the area of the coseismic rupture in the Iquique earthquake (Fig. S6a). Postseismic VER exerts a positive stress change that overlaps with the Iquique rupture, but is mostly downdip of it (Fig. S7a). For the plate interface down to a depth of 40 km, stress loading due to postseismic VER is negative. Taken together, the combined stress loading is mostly negative on the Iquique mainshock rupture, showing that the postseismic Tarapaca VER process dominates the Coulomb stress change across the Iquique rupture on the plate interface. On the nodal planes of the M 6.7 preshock, the coseismic stress loading (Fig. S6b and c) from the Tarapaca earthquake is ~ 8 times larger than that from the postseismic VER process (Fig. S7b and c). The combined stress change projected on the shallow-dipping nodal plane of the preshock is positive and reaches ~ 5 kPa. As mentioned earlier, the M 6.7 preshock positively loaded the 2014 Iquique rupture plane (Hayes et al., 2014). Together, these lines of enquiry imply that, via loading of the M 6.7 preshock fault, the static stress change from the Tarapaca earthquake may have acted as an indirect trigger for the Iquique earthquake. At a late stage of the earthquake cycle when interseismic stress accumulation is high, even a small stress perturbation may initiate the subsequent failure of a long-coupled segment.

5. Conclusions

We take advantage of InSAR and GPS measurements covering the 2005 intraslab Tarapaca earthquake epicentral area in North Chile, before and after the main shock, to investigate the related postseismic relaxation effect. Our study demonstrates that such a deep normal faulting intraslab earthquake generates a measurable deformation at the surface that helps constrain the subduction zone rheology. We show that a continental asthenosphere with viscosity of $4 - 8 \times 10^{18}$ Pa s underlying the lower crust, together with a mantle lithosphere of viscosity $> 5 \times 10^{19}$ Pa s and a strong forearc zone for the continental part, retrieve well the observed deformation pattern in North Chile. Calculation of Coulomb stress change on the 2014 Iquique rupture and its preshock nodal planes indicates that the static stress change from the Tarapaca earthquake and its postseismic VER may have acted as an indirect trigger for the Iquique earthquake, shedding new light on the overall sequence of seismic activity.

Acknowledgements

MERIS data and ECMWF ERA-Interim data are from the British Atmospheric Data Centre (BADC). We thank all the researchers, engineers and students from French-Chilean LiA Montessus de Ballore (LIA-MB) that took part in the GPS fieldwork, in particular J.C Ruegg who installed the first network, and C. Vigny and A. Socquet who subsequently developed the network. We thank Roland Burgmann for valuable comments on an early version of this manuscript.

References

Altamimi, Z., Collilieux, X. & Métivier, L., 2011. ITRF2008: an improved solution of the international terrestrial reference frame. J. Geod., 85(8), 457-473.

Argus, D. F., Gordon, R. G. & DeMets, C., 2011. Geologically current motion of 56 plates relative to the no-net-rotation reference frame. Geochemistry, Geophysics, Geosystems, 12(11). DOI: 10.1029/2011GC003751.

Astiz, L., Lay, T. & Kanamori, H., 1988. Large intermediate-depth earthquakes and the subduction process, Phys. Earth planet. Inter., 53(1), 80-166.

Barbot, S. & Fialko, Y., 2010. A unified continuum representation of post-seismic relaxation mechanisms: semi-analytic models of afterslip, poroelastic rebound and viscoelastic flow. Geophys. J. Int., 182(3), 1124-1140.

Bennartz, R. & Fischer, J., 2001. Retrieval of columnar water vapour over land from backscattered solar radiation using the Medium Resolution Imaging Spectrometer. Remote Sens. Environ., 78(3), 274-283.

Béjar-Pizarro, M., Socquet, A., Armijo, R., Carrizo, D., Genrich, J. & Simons, M., 2013. Andean structural control on interseismic coupling in the North Chile subduction zone. *Nature Geoscience*, 6(6), 462-467.

Bürgmann, R. & Dresen, G., 2008. Rheology of the lower crust and upper mantle: Evidence from rock mechanics, geodesy, and field observations. Annu. Rev. Earth planet Sci., 36(1), 531.

Bürgmann, R., 2014. Earth science: Warning signs of the Iquique earthquake. Nature, 512, 258-259. doi:10.1038/nature13655.

Chlieh, M., De Chabalier, J. B., Ruegg, J. C., Armijo, R., Dmowska, R., Campos, J. & Feigl, K. L., 2004. Crustal deformation and fault slip during the seismic cycle in the North Chile subduction zone, from GPS and InSAR observations. Geophys. J. Int., 158(2), 695-711.

Chlieh, M., Perfettini, H., Tavera, H., Avouac, J. P., Remy, D., Nocquet, J. M. & Bonvalot, S., 2011. Interseismic coupling and seismic potential along the Central Andes subduction zone. J. Geophys. Res., 116(B12), Doi: 10.1029/2010JB008166.

DeMets, C., Gordon, R. G., Argus, D. F. & Stein, S., 1994. Effect of recent revisions to the geomagnetic reversal time scale on estimates of current plate motions. Geophys. Res. lett., 21(20), 2191-2194.

Ding, M. & Lin, J., 2014. Post-seismic viscoelastic deformation and stress transfer after the 1960 M9. 5 Valdivia, Chile earthquake: effects on the 2010 M8. 8 Maule, Chile earthquake. Geophys. J. Int., DOI: 10.1093/gji/ggu048.

Farr et al., 2007. The shuttle radar topography mission. Rev. Geophys., 45(2).

Feng, L., Newman, A. V., Protti, M., González, V., Jiang, Y. & Dixon, T. H., 2012. Active deformation near the Nicoya Peninsula, northwestern Costa Rica, between 1996 and 2010: Interseismic megathrust coupling. J. Geophys. Res., 117(B6).

Fuenzalida, A., Tavera, H., Ruiz, S., Ryder, I., Fernandez, E., Garth, T., Neto, O. D. L., Métois, M., De Angelis, S. & Rietbrock, A., 2014. Nucleation of the 2014 Pisagua, N. Chile earthquake: seismic analysis of the foreshock sequence. American Geophysical Union, Fall Meeting 2014. Abstract #S31D-4456.

Gardi, A., Lemoine, A., Madariaga, R. & Campos, J., 2006. Modeling of stress transfer in the Coquimbo region of central Chile. J. Geophys. Res., 111(B4), Doi:10.1029/2004JB003440.

Goldstein, R. M., Zebker, H. A. & Werner, C. L., 1988. Satellite radar interferometry: Two-dimensional phase unwrapping, *Radio Sci.*, 23(4), 713-720.

Hayes, G. P., Herman, M. W., Barnhart, W. D., Furlong, K. P., Riquelme, S., Benz, H. M., Bergman, E., Barrientos, S., Earle, P. & Samsonov, S., 2014. Continuing megathrust earthquake potential in Chile after the 2014 Iquique earthquake. Nature, 512(7514), 295-298.

Hetland, E. A. & Zhang, G., 2014. Effect of shear zones on post-seismic deformation with application to the 1997 Mw 7.6 Manyi earthquake. Geophys. J. Int., doi: 10.1093/gji/ggu127.

Hu, Y. & Wang, K., 2012. Spherical-Earth finite element model of short-term postseismic deformation following the 2004 Sumatra earthquake. J. Geophys. Res., 117(B5).

Jolivet, R., Agram, P. S., Lin, N. Y., Simons, M., Doin, M. P., Peltzer, G. & Li, Z., 2014. Improving InSAR geodesy using global atmospheric models. J. Geophys. Res., 119(3), 2324-2341.

Kausel, E. & Campos, J., 1992. The Ms = 8 tensional earthquake of 9 December 1950 of northern Chile and its relation to the seismic potential of the region. Phys. Earth planet. Inter., 72(3), 220-235.

King, R. W. & Bock, Y., 2002. Documentation for the GAMIT Analysis Software, release 10.0. Massachusetts Institute of Technology, Cambridge, MA.

Klein, E., Fleitout, L., Vigny, C. & Garaud, J. D., 2016. Afterslip and viscoelastic relaxation model inferred from the large scale postseismic deformation following the 2010 Mw8.8 Maule earthquake (Chile). Geophys. J. Int., doi: 10.1093/gji/ggw086.

Lay, T., Astiz, L., Kanamori, H. & Christensen, D. H., 1989. Temporal variation of large intraplate earthquakes in coupled subduction zones. Phys. Earth planet. Inter., 54(3), 258-312.

Li, Z., Muller, J. P., Cross, P., Albert, P., Fischer, J. & Bennartz, R., 2006. Assessment of the potential of MERIS near-infrared water vapour products to correct ASAR interferometric measurements. Int. J. Remote Sens., 27(2), 349-365.

Loveless, J. P. & Meade., 2016. Two decades of spatiotemporal variations in subduction zone coupling offshore Japan. Earth planet Sci. Lett., 436, 19-30. DOI: 10.1016.j.epsl.2015.12.033.

Mavrommatis, A. P., Segall, P. & Johnson, K. M., 2014. A decadal-scale deformation transient prior to the 2011 M_w 9.0 Tohoku-Oki earthquake. Geophys. Res. Lett., 41(13), 4486-4494.

Métois, M., Socquet, A., Vigny, C., Carrizo, D., Peyrat, S., Delorme, A., Maureira, E., Valderas-Bermejo, M.-C. & Ortega, I., 2013. Revisiting the North Chile seismic gap segmentation using GPS-derived interseismic coupling. Geophys. J. Int., 194(3), 1283-1294.

Nishimura, T., Hirasawa, T., Miyazaki, S. I., Sagiya, T., Tada, T., Miura, S. & Tanaka, K., 2004. Temporal change of interplate coupling in northeastern Japan during 1995-2002 estimated from continuous GPS observations. Geophys. J. Int., 157(2), 901-916.

Peyrat, S., Campos, J., De Chabalier, J. B., Perez, A., Bonvalot, S., Bouin, M. P., Legrand, D., Nercessian, A., Charade, O., Patau, G., Clévédé, E., Kausel, E., Bernard, P. & Vilotte, J. P., 2006. Tarapacá intermediate-depth earthquake (M_w 7.7, 2005, northern Chile): A slab-pull event with horizontal fault plane constrained from seismologic and geodetic observations. Geophys. Res. Lett., 33(22).

Pollitz, F., Banerjee, P., Grijalva, K., Nagarajan, B. & Bürgmann, R., 2008. Effect of 3-D viscoelastic structure on post-seismic relaxation from the 2004 M = 9.2 Sumatra earthquake. Geophys. J. Int., 173(1), 189-204.

Rosen, P. A., Henley, S., Peltzer, G. & M. Simons (2004), Update repeat orbit interferometry package released, Eos Trans. AGU, 85, 47, doi:10.1029/2004EO050004.

Ruegg, J. C., Campos, J., Armijo, R., Barrientos, S., Briole, P., Thiele, R., Arancibia, M., Canuta, J., Duquesnoy, T., Chang, M., Lazo, D., Lyon-Caen, H., Ortlieb, L., Rossignol, J. C. & Serrurier, L., 1996. The Mw = 8.1 Antofagasta (North Chile) earthquake of July 30, 1995: First results from teleseismic and geodetic data. Geophys. Res. Lett., 23(9), 917-920.

Ruiz, S., Metois, M., Fuenzalida, A., Ruiz, J., Leyton, F., Grandin, R., Vigny, C., Madariaga, R. & Campos, J., 2014. Intense foreshocks and a slow slip event preceded the 2014 Iquique M_w 8.1 earthquake. Science, 345(6201), 1165-1169.

Schurr, B., Asch, G., Rietbrock, A., Trumbull, R. & Haberland, C. H., 2003. Complex patterns of fluid and melt transport in the central Andean subduction zone revealed by attenuation tomography. Earth planet Sci. Lett., 215(1), 105-119.

Schurr, B. & Rietbrock, A., 2004. Deep seismic structure of the Atacama basin, northern Chile. Geophys. Res. Lett., 31(12).

Schurr, B., Asch, G., Hainzl, S., Bedford, J., Hoechner, A., Palo, M., Wang, R., Moreno, M., Bartsch, M., Zhang, Y., Oncken, O., Tilmann, F., Dahm, T., Victor, P., Barrientos, S. & Vilotte, J. P., 2014. Gradual unlocking of plate boundary controlled initiation of the 2014 Iquique earthquake. Nature, 512, 299-302. doi:10.1038/nature13681.

Steacy, S., Gomberg, J. & Cocco, M., 2005. Introduction to special section: Stress transfer, earthquake triggering, and time-dependent seismic hazard. J. Geophys. Res., 110(B5).

Sun, T., Wang, K., Iinuma, T., Hino, R., He, J., Fujimoto, H., Kido, M., Osada, Y., Miura, S., Ohta, Y. & Hu, Y., 2014. Prevalence of viscoelastic relaxation after the 2011 Tohoku-oki earthquake. Nature, 514(7520), 84-87.

Trubienko, O., Garaud, J. D. & Fleitout, L., 2014. Models of postseismic deformation after megaearthquakes: the role of various rheological and geometrical parameters of the subduction zone. *Solid Earth Discussions*, 6(1), 427-466.

Walters, R. J., Elliott, J., Li, Z. & Parsons, B., 2013. Rapid strain accumulation on the Ashkabad fault (Turkmenistan) from atmosphere-corrected InSAR, J. Geophys. Res., 118, 3674–3690, doi:10.1002/jgrb.50236.

Wada, I., & Wang, K., 2009. Common depth of slab-mantle decoupling: Reconciling diversity and uniformity of subduction zones. Geochemistry, Geophysics, Geosystems, 10(10).

Wang, K., Hu, Y. & He, J., 2012. Deformation cycles of subduction earthquakes in a viscoelastic Earth. Nature, 484(7394), 327-332.

Figures

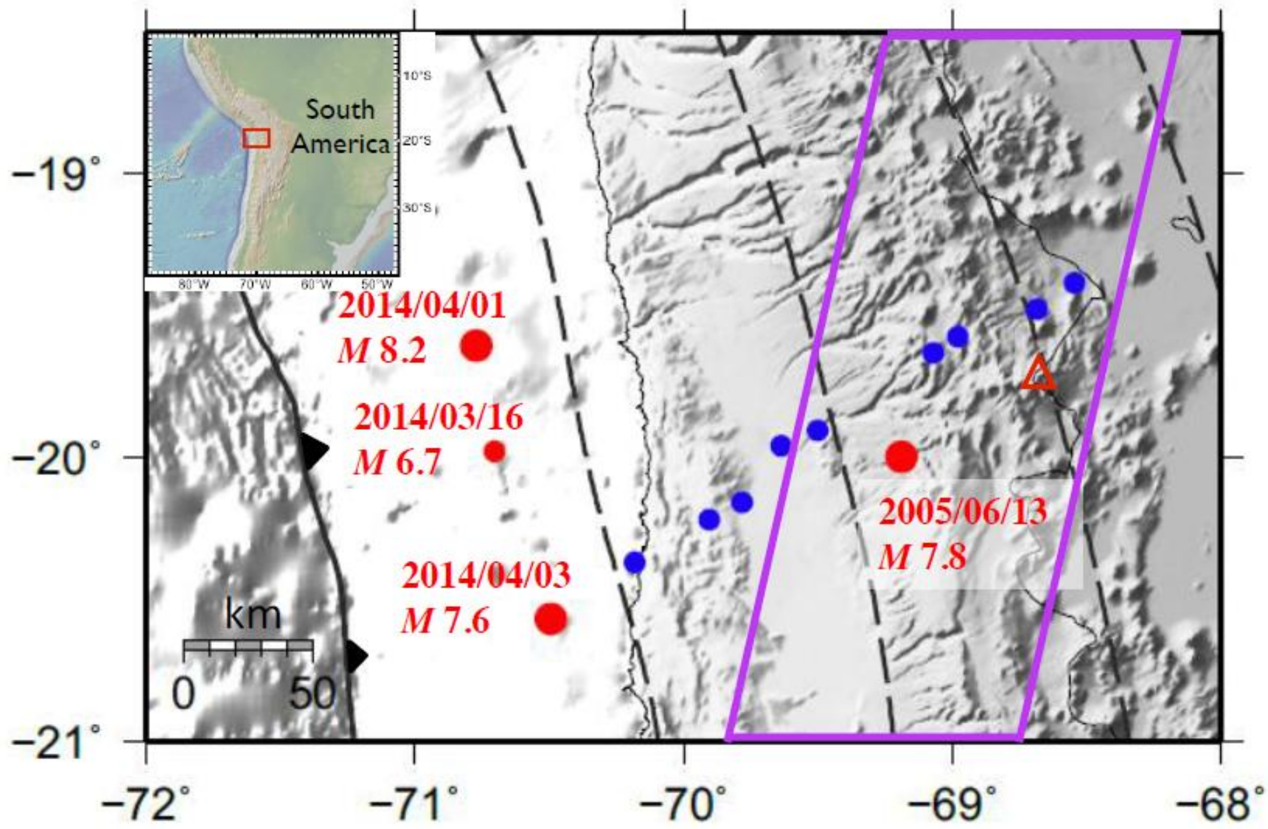

Fig. 1. Topographic map of the northern Chile subduction zone. Grey dashed lines delineate the slab contours at 40 km depth intervals (Hayes et al., 2012). Red dots mark the locations of earthquakes in this study. Red triangle marks the location of the Sillajhuay volcano. Blue dots are survey-mode GPS locations (Métois et al., 2013). Purple lines delineate the area covered by InSAR data shown in Fig. 2. Inset figure shows the study region relative to South America.

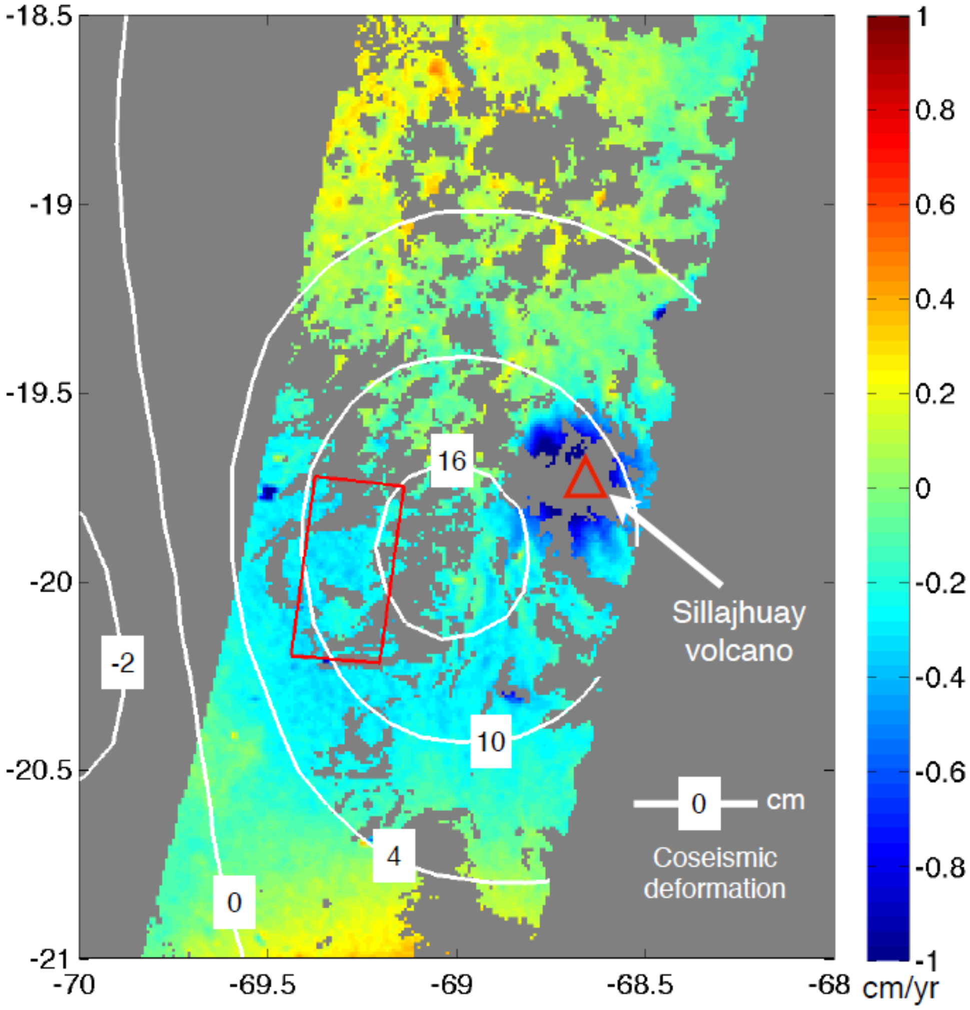

Fig. 2. Rate map constructed from postseismic Envisat interferograms from June 2005 to March 2009, as listed in Table S2. Warm colours indicate LOS motion away from the satellite. Coseismic deformation of the Tarapaca earthquake is shown by white contours, with positive values representing motion away from the satellite. Red rectangle is the surface projection of the Tarapaca rupture from Peyrat et al. (2006). Red triangle marks the location of the Sillajhuay volcano.

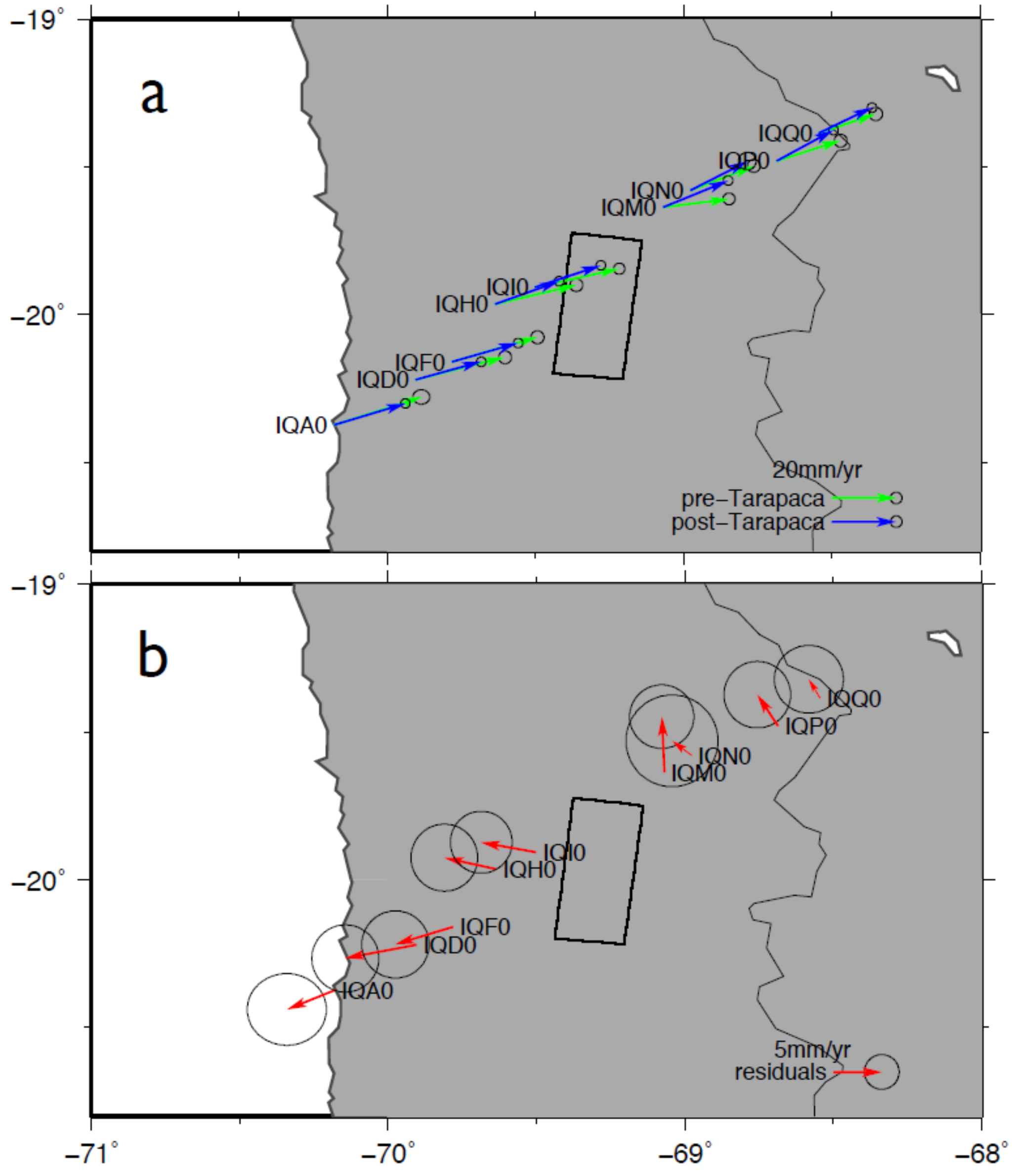

Fig. 3. (a) Horizontal velocities relative to stable South America from survey mode GPS measurements before (1996, 2000) and after (2005, 2010, 2012) the Tarapaca earthquake. Velocity vectors are tipped by the 80% confidence ellipses. (b) Difference between the pre- and post-mainshock displacements shown in (a) (see Table S3 - S5). Black rectangle is the surface projection of the Tarapaca rupture from Peyrat et al. (2006)

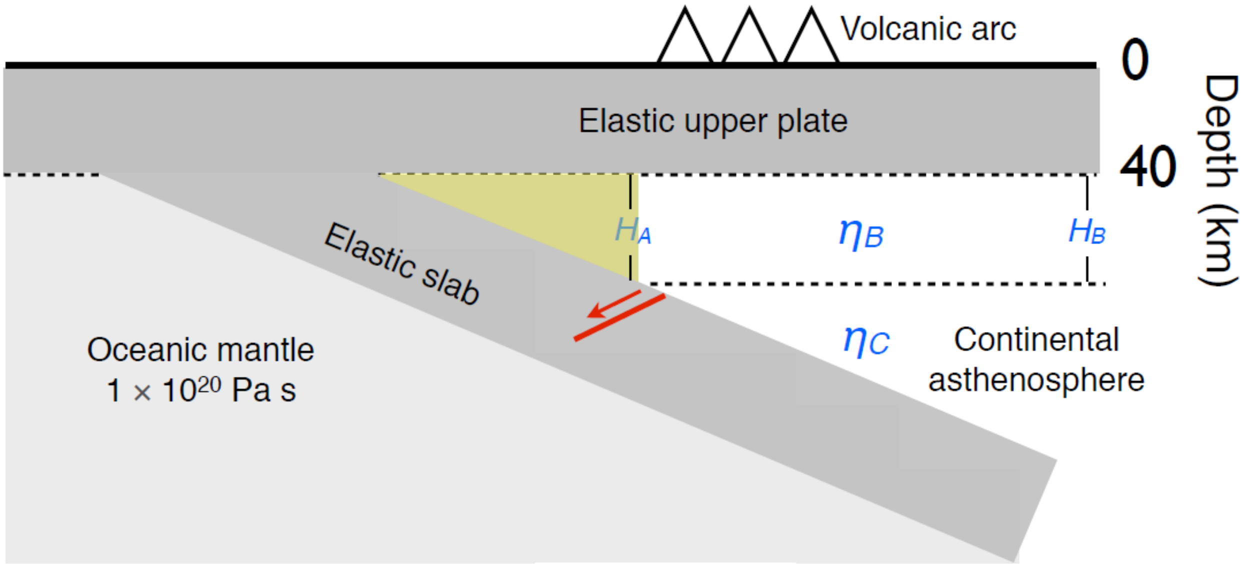

Fig. 4. Schematic cross-section perpendicular to the trench, showing the rheological structure constrained in this study. Yellow triangle represents the cold and stagnant part of the forearc (zone A). Parameters **(**H_A, H_B, η_B and η_C**)** in blue are variables to infer. Oceanic mantle viscosity is fixed, but its effect on surface deformation is tested and shown in Fig. S2.

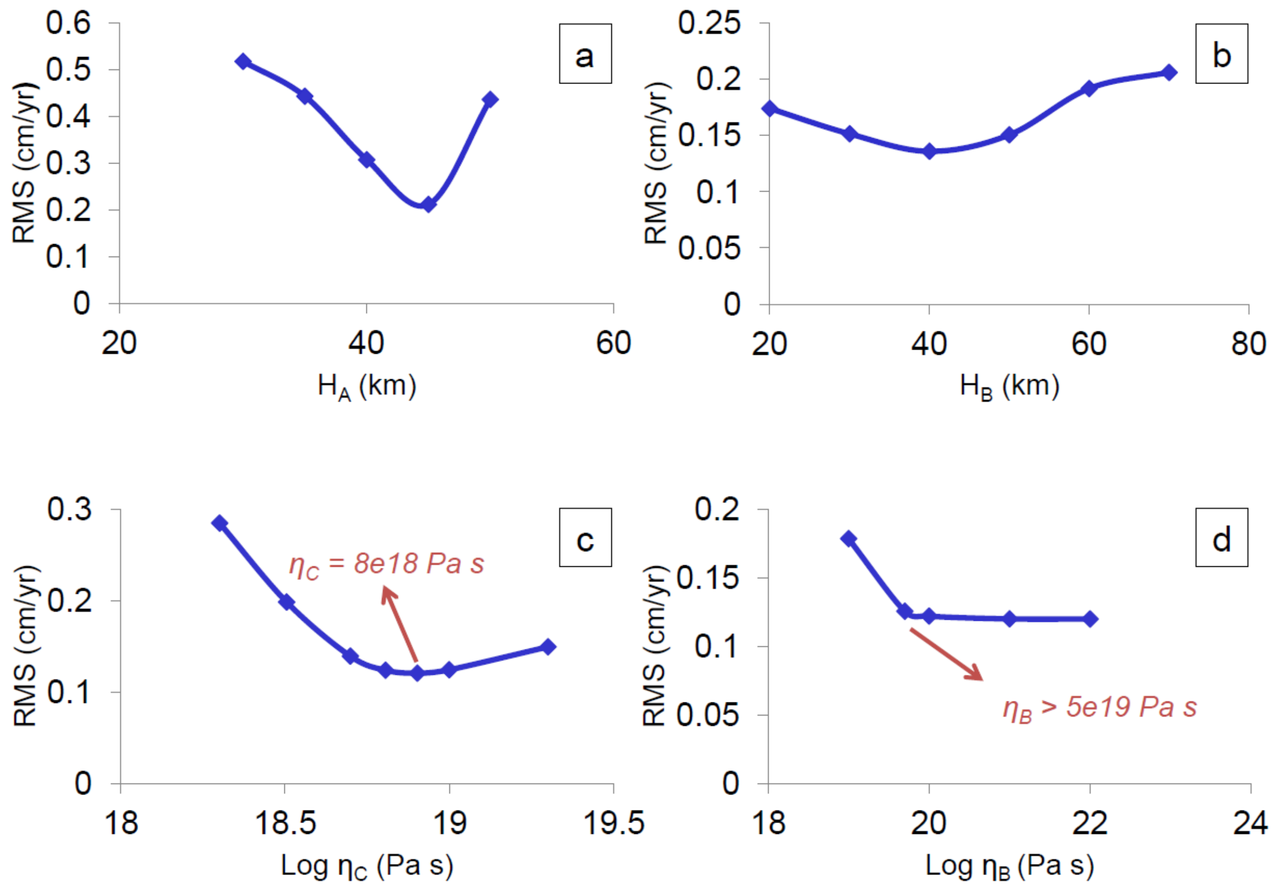

Fig. 5. RMS misfit curves derived during modelling. (a) RMS misfit versus thickness of zone A. Zone B and C are viscoelastic layers with fixed viscosity of 4×10^{18} Pa s. (b) RMS misfit versus thickness of zone B. Zone B is fixed as being elastic, while η_C is 4×10^{18} Pa s. (c) RMS misfit versus viscosity of zone C, holding A and B fixed at thicknesses and viscosities preferred in (a) and (b). (d) RMS misfit versus viscosity of zone B. Viscosity of zone C is fixed at 8×10^{18} Pa s, as derived in Fig 5(c).

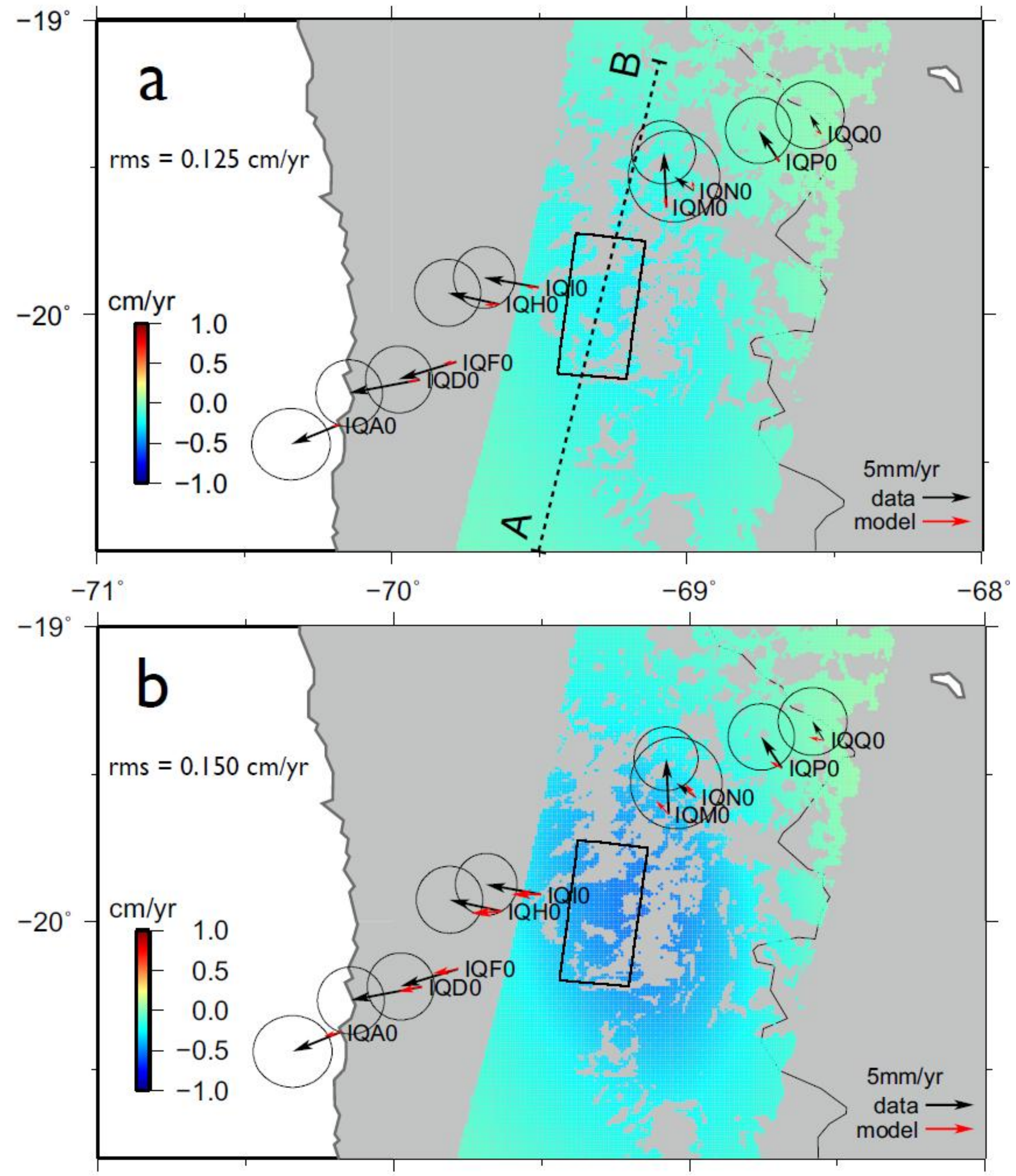

Fig. 6. Modelled rate map of InSAR LOS displacement and GPS horizontal displacements (red arrows) with zone C viscosity η_C of: (a) 8 $\times 10^{18}$ Pa s; (b) 4 $\times 10^{18}$ Pa s. Other parameters are: $H_A = H_B = 45$ km, $\eta_B = 5 \times 10^{19}$ Pa s. Black arrows are the same as shown in Fig. 3(b). Black dashed line marked as A-B in (a) denotes the profile in Fig. 8. RMS misfit between model and InSAR data is given in units of cm/yr. Fig. 6(a) is reproduced in Fig. S8, but with the modelled GPS displacement scaled by 4 times, in order to clearly show the agreement in azimuth.

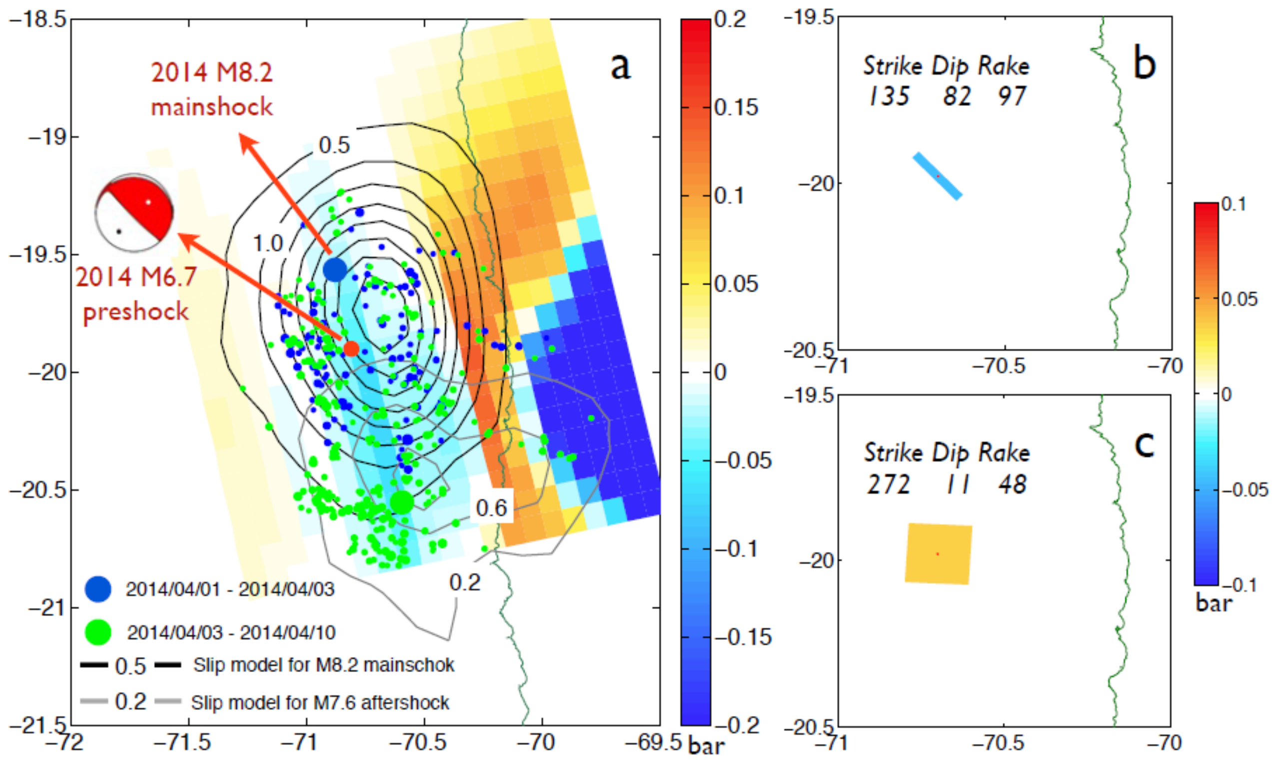

Fig. 7. Coulomb stress changes induced by the co- and postseismic deformation associated with the Tarapaca earthquake. (a) Stress change on the subduction interface. Aftershock distribution and slip models for the *M* 8.2 Iquique earthquake and its *M* 7.6 aftershock, are from Schurr et al. (2014). (b) and (c) Stress change on the nodal planes of the *M* 6.7 foreshock.

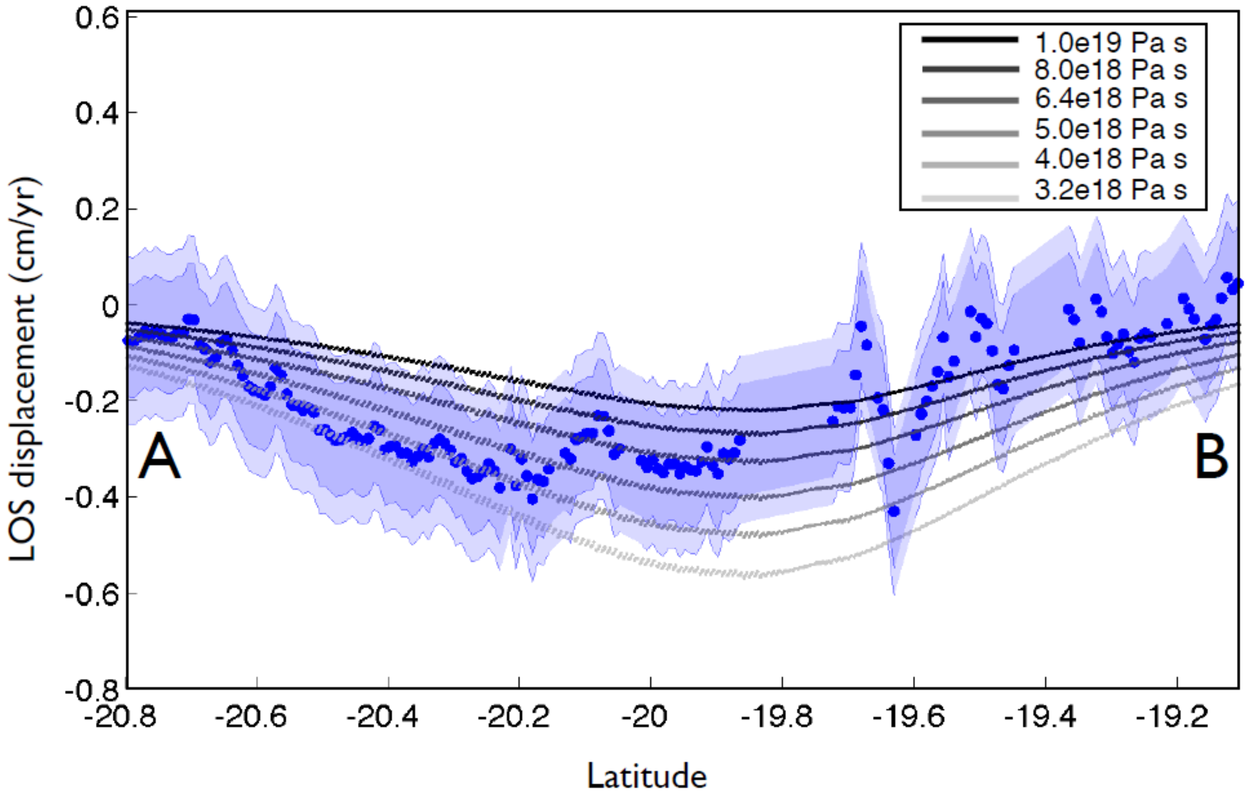

Fig. 8. LOS displacement changes with different viscosity for the continental asthenosphere along the A-B profile shown in Fig. 6(a). Blue dots show the LOS displacement rate along the profile. Higher viscosities provide a better a better fit to the northern part of the zone. The inner error bound (deep blue area) is a theoretical standard deviation derived from estimates by Li et al. (2006) of the MERIS data accuracy, and the outer bound (light blue area) is from Bennartz & Fischer (2001).

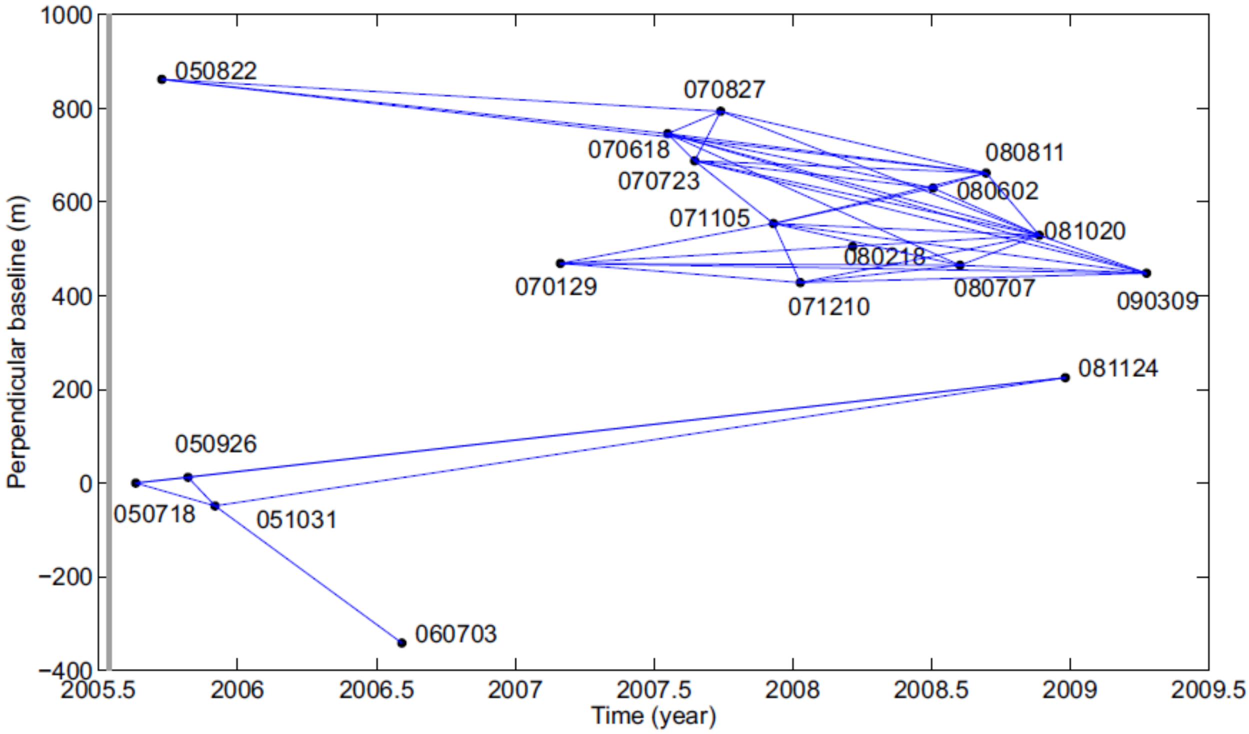

Fig. S1. Perpendicular baseline-time plots for the 45 Envisat interferograms (Table S2) used for rate map construction. Grey line marks the Tarapaca earthquake on 13 June 2005.

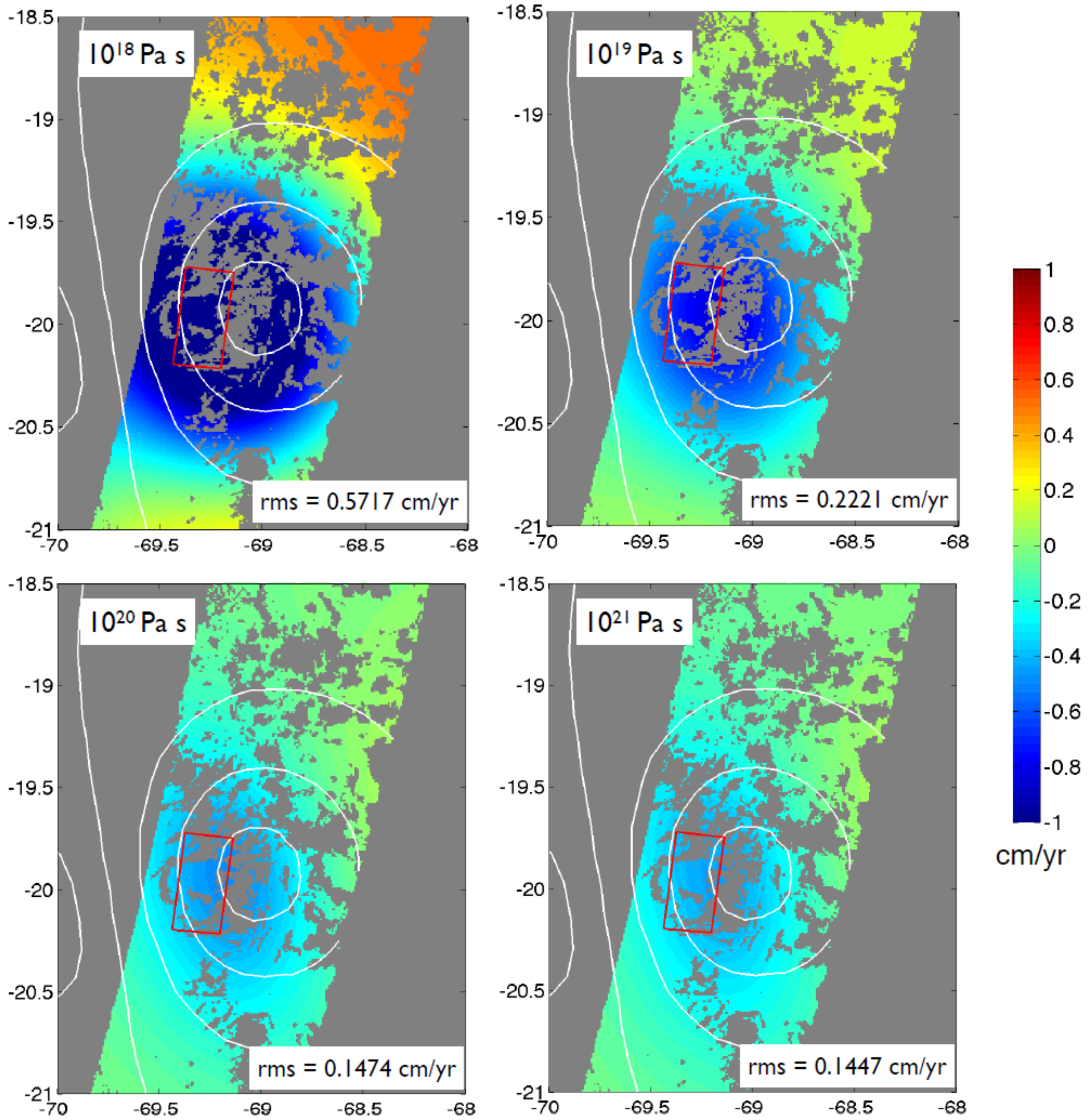

Fig. S2. Modelled LOS displacements with various viscosity inputs for the oceanic mantle. Oceanic mantle viscosity is shown in top-left corner of each subfigure. Other parameters are same as used for Fig. 6(b). Warm colours indicate LOS motion away from the satellite. Coseismic deformation of the Tarapaca earthquake is shown by the same white contours as in Fig. 2. Red rectangle is the surface projection of the Tarapaca rupture from Peyrat et al. (2006). RMS misfit between InSAR model and data is given for each case in the lower right corner.

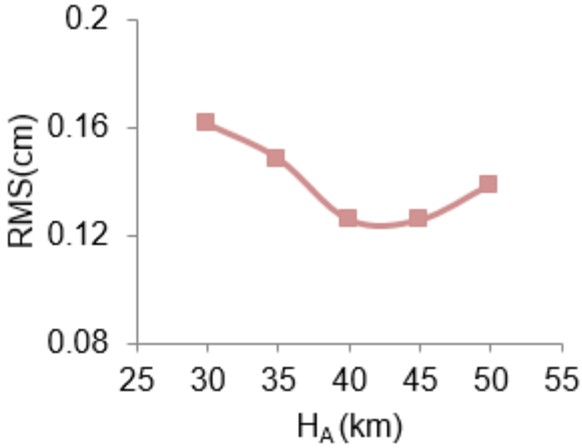

Fig. S3. RMS misfit versus thickness of Zone A. We assign 5 ×10[19] Pa s and 8 ×10[18] Pa s for η_B and η_C respectively, as derived from progressive tests shown in Fig. 5. This plot shows convergence with result in the first step, where the optimal thickness for zone A is 45 km.

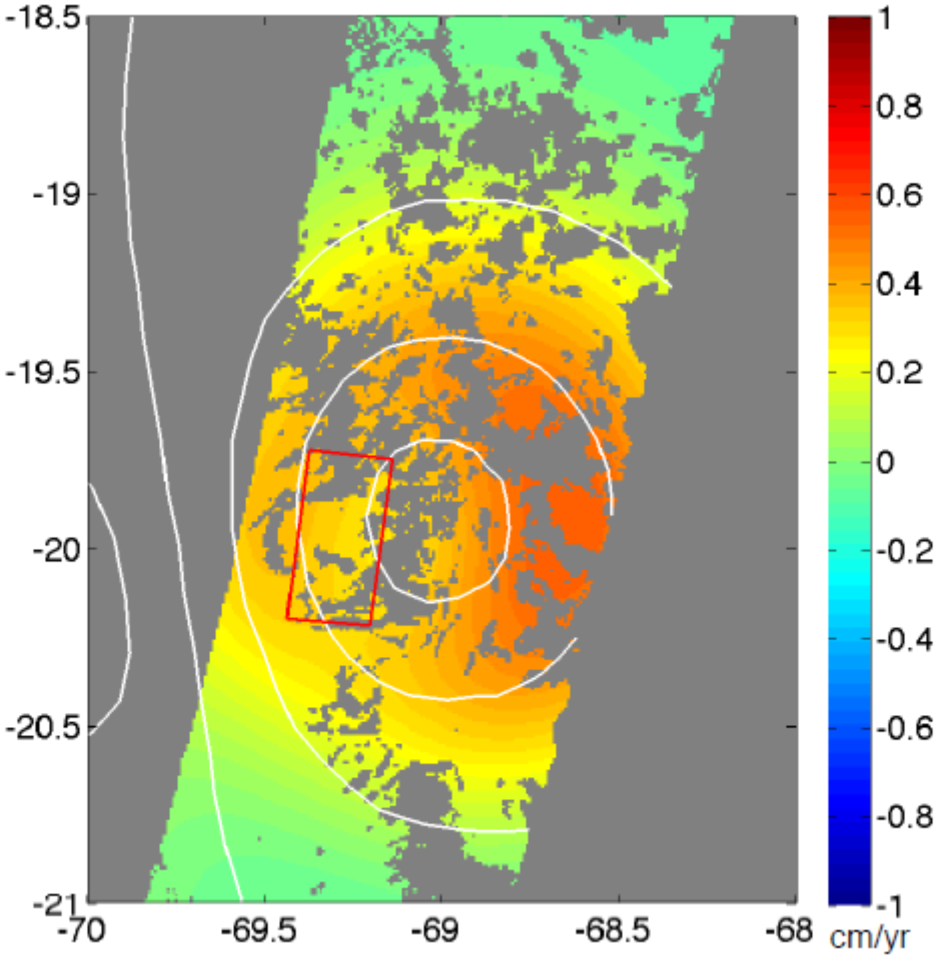

Fig. S4. Forward modeled LOS displacement with a viscoelastic zone A, sharing same viscosity as zone B and C (4×10^{18} Pa s).

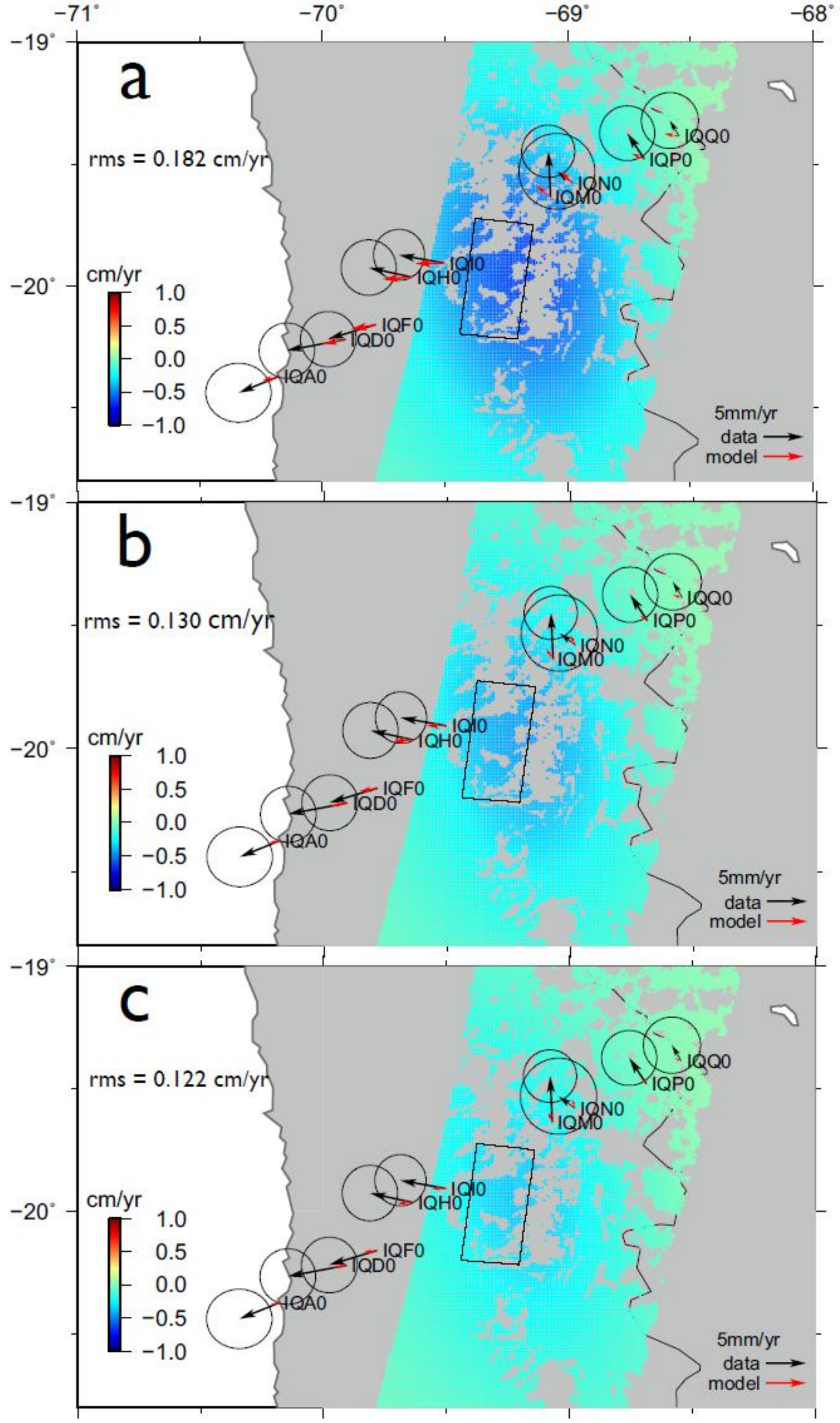

Fig. S5. Modelled rate map of InSAR LOS displacement and GPS horizontal displacements (red arrows) with zone C viscosity of: (a) 3.2 $\times 10^{18}$ Pa s; (b) 5 $\times 10^{18}$ Pa s; (c) 6.4 $\times 10^{18}$ Pa s. Other parameters are: $H_A = H_B = 45$ km, $\eta_B = 5 \times 10^{19}$ Pa s. Black arrows are the same as shown in Fig. 3(b). RMS misfit between model and data is given with unit cm/yr.

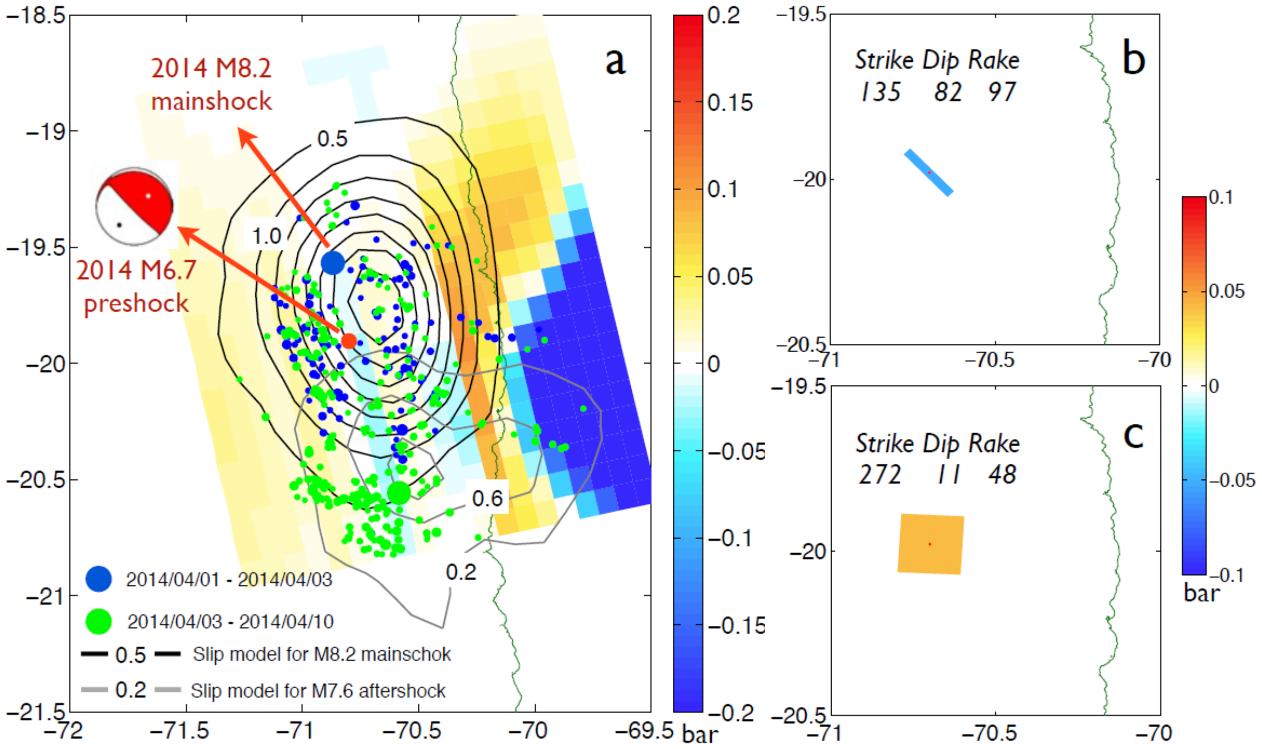

Fig. S6. Coulomb stress changes induced by the coseismic rupture of the Tarapaca earthquake only. (a) Stress change on the subduction interface. Aftershock distribution, and slip models for *M* 8.2 Iquique earthquake and its *M* 7.6 aftershock, are from Schurr et al. (2014). (b) and (c) Stress change resolved on the nodal planes of the *M* 6.7 preshock.

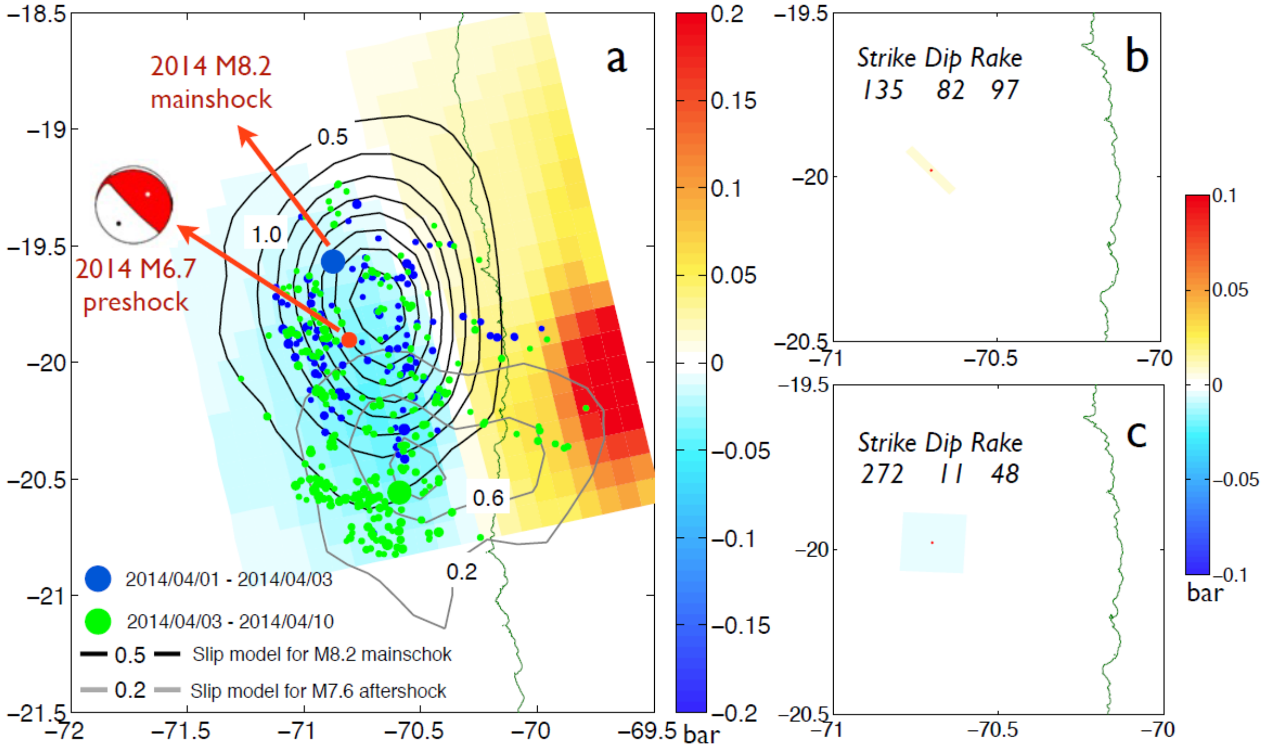

Fig. S7. Coulomb stress changes induced by the postseismic VER after the Tarapaca earthquake only. (a) Stress change on the subduction interface. Aftershock distribution, and slip models for *M* 8.2 Iquique earthquake and its *M* 7.6 aftershock, are from Schurr et al. (2014). (b) and (c) Stress change resolved on the nodal planes of the *M* 6.7 preshock.

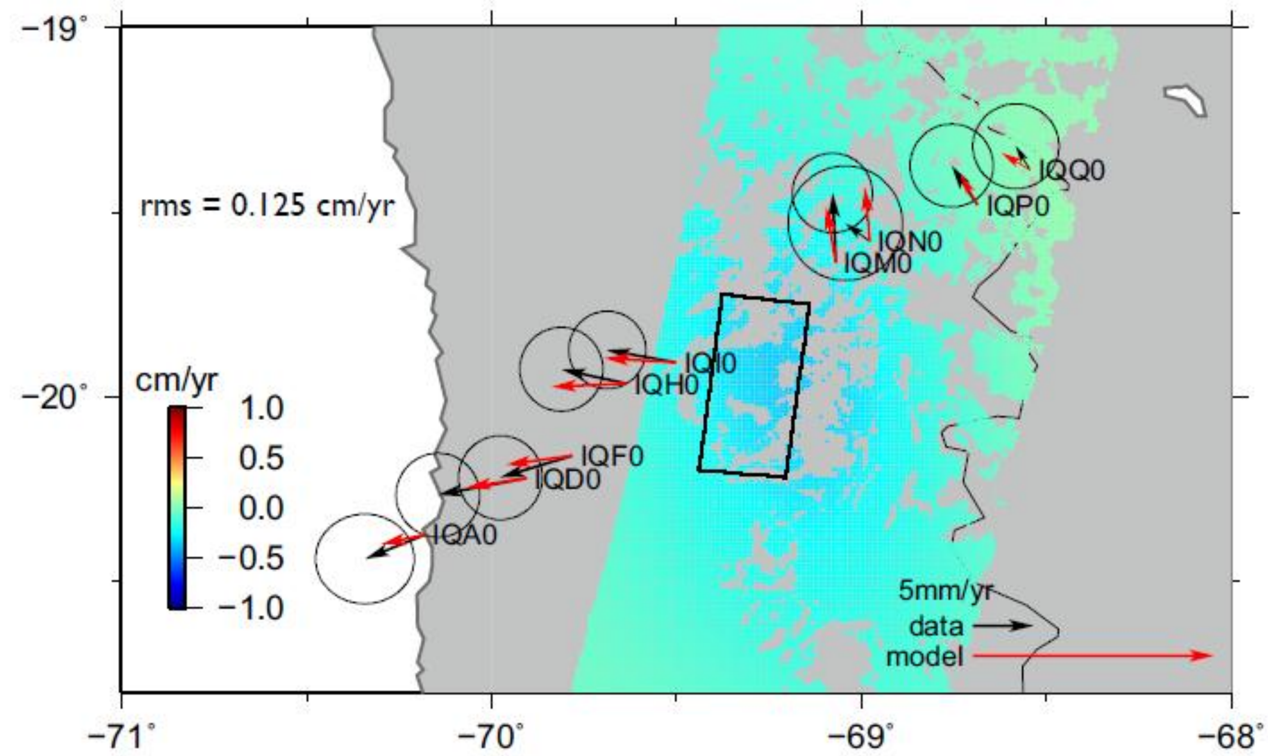

Fig. S8. A reproduction of Fig. 6. Modelled rate map of InSAR LOS displacement and GPS horizontal displacements (red arrows) with zone C viscosity of 8×10^{18} Pa s. In comparison to Fig. 6(a), modelled GPS horizontal displacements in Fig. S8 are scaled up by 4 times, in order to clearly show the agreement with data in azimuth.

Tables

Table S1. Source parameters of the 2005 Mw 7.8 Tarapaca earthquake (Peyrat et al., 2006), used as input for VER modelling.

Length (km)	Width (km)	Top depth (km)	Strike	Dip	Rake	Slip (m)
54	24	90	189	24	-74	6.5

Table S2. List of postseismic interferograms stacked for rate map.

Postseismic interferogram pairs (yymmdd - yymmdd)
050718 - 050926
050718 - 051031
050718 - 081124
050822 - 070618
050822 - 070827
050822 - 080811
050926 - 051031
050926 - 081124
051031 - 060703
051031 - 081124
070129 - 071105
070129 - 071210
070129 - 080707
070129 - 081020
070129 - 090309
070618 - 070723
070618 - 070827

070618 - 080602
070618 - 080707
070618 - 080811
070618 - 081020
070618 - 090309
070723 - 070827
070723 - 071105
070723 - 080602
070723 - 080811
070723 - 081020
070723 - 090309
070827 - 080811
070827 - 081020
071105 - 071210
071105 - 080602
071105 - 080707
071105 - 080811
071105 - 081020
071105 - 090309
071210 - 080707
071210 - 081020
071210 - 090309

080602 - 080811
080602 - 081020
080707 - 081020
080707 - 090309
080811 - 081020
081020 - 090309

Table S3. Pre-Tarapaca GPS velocities in mm/yr relative to stable South America as defined by NNR-Nuvel1A model. The original velocities were calculated in ITRF2008.

STATION	LON	LAT	Ve	Vn	σe	σn	Measurements	Time-span
IQA0	-70.18	-20.373	27.19	8.72	1.46	1.25	2	1996.915- 2000.8
IQD0	-69.904	-20.221	27.78	7.05	1.11	1.12	2	1996.915-2000.8
IQF0	-69.781	-20.160	26.51	7.70	1.12	1.12	2	1996.915-2000.8
IQH0	-69.636	-19.964	25.23	5.93	1.11	1.12	2	1996.915-2000.8
IQI0	-69.501	-19.907	26.13	5.75	0.96	0.97	3	1996.915-2002.556
IQM0	-69.07	-19.636	20.54	2.55	1.03	1.02	3	1996.915-2002.556
IQN0	-68.978	-19.579	19.78	7.56	1.12	1.12	2	1996.915-2000.8
IQP0	-68.686	-19.481	19.87	6.39	1.11	1.11	2	1996.915-2000.8
IQQ0	-68.544	-19.387	17.71	6.03	1.17	1.14	2	1996.915-2000.8

Table S4. Post Tarapaca GPS velocities in mm/yr relative to stable South America as defined by NNR-Nuvel1A model. The original velocities were calculated in ITRF2008.

STATION	LON	LAT	Ve	Vn	σe	σn	Measurements	Time-span
IQA0	-70.18	-20.373	22.22	6.70	0.82	0.82	3	2005.501-2012.288
IQD0	-69.904	-20.221	20.40	5.66	0.82	0.82	2	2005.501-2012.288
IQF0	-69.781	-20.160	20.54	5.89	0.82	0.82	3	2005.501-2012.288
IQH0	-69.636	-19.964	19.86	7.11	0.81	0.82	3	2005.501-2012.288
IQI0	-69.501	-19.907	20.43	6.78	0.82	0.82	3	2005.501-2012.288
IQM0	-69.07	-19.636	20.28	8.30	0.82	0.82	3	2005.501-2012.288
IQN0	-68.978	-19.579	17.76	9.05	1.53	1.53	2	2010.458-2012.288
IQP0	-68.686	-19.481	17.71	9.66	0.81	0.81	3	2005.501-2012.288
IQQ0	-68.544	-19.387	16.53	8.02	0.82	0.82	3	2005.501-2012.288

Table S5. Residual velocities (post-pre Tarapaca earthquake) in mm/yr interpreted as postseismic deformation in this study. Velocities are relative to stable South America as defined by NNR-Nuvel1A model.

STATION	LON	LAT	Re	Rn	σre	σrn
IQA0	-70.18	-20.373	-4.97	-2.02	2.28	2.07
IQD0	-69.904	-20.221	-7.38	-1.39	1.93	1.94
IQF0	-69.781	-20.160	-5.97	-1.81	1.94	1.94
IQH0	-69.636	-19.964	-5.37	1.18	1.92	1.94
IQI0	-69.501	-19.907	-5.7	1.03	1.78	1.79
IQM0	-69.07	-19.636	-0.26	5.75	1.85	1.84
IQN0	-68.978	-19.579	-2.02	1.49	2.65	2.65
IQP0	-68.686	-19.481	-2.16	3.27	1.92	1.92
IQQ0	-68.544	-19.387	-1.18	1.99	1.99	1.96